Computer Methods and Programs in Biomedicine 237 (2023) 107569

Contents lists available at ScienceDirect

Computer Methods and Programs in Biomedicine

journal homepage: www.elsevier.com/locate/cmpb

Four-dimensional reconstruction and characterization of bladder deformations

Augustin C. Ogier[a,*], Stanislas Rapacchi[b], Marc-Emmanuel Bellemare[a]

[a] Aix Marseille Univ, Universite de Toulon, CNRS, LIS, Marseille, France
[b] Aix Marseille Univ, CNRS, CRMBM, Marseille, France

ARTICLE INFO

Article history:
Received 14 March 2022
Revised 31 March 2023
Accepted 24 April 2023

Keywords:
3D Dynamic MRI
Bladder
Pelvic dynamics
Volume reconstruction

ABSTRACT

Background and Objective: Pelvic floor disorders are prevalent diseases and patient care remains difficult as the dynamics of the pelvic floor remains poorly understood. So far, only 2D dynamic observations of straining exercises at excretion are available in the clinics and 3D mechanical defects of pelvic organs are not well studied. In this context, we propose a complete methodology for the 3D representation of non-reversible bladder deformations during exercises, combined with a 3D representation of the location of the highest strain areas on the organ surface.

Methods: Novel image segmentation and registration approaches have been combined with three geometrical configurations of up-to-date rapid dynamic multi-slice MRI acquisitions for the reconstruction of real-time dynamic bladder volumes.

Results: For the first time, we proposed real-time 3D deformation fields of the bladder under strain from in-bore forced breathing exercises. The potential of our method was assessed on eight control subjects undergoing forced breathing exercises. We obtained average volume deviations of the reconstructed dynamic volume of bladders around 2.5% and high registration accuracy with mean distance values of 0.4 $\pm$ 0.3 mm and Hausdorff distance values of 2.2 $\pm$ 1.1 mm.

Conclusions: The proposed framework provides proper 3D+t spatial tracking of non-reversible bladder deformations. This has immediate applicability in clinical settings for a better understanding of pelvic organ prolapse pathophysiology. This work can be extended to patients with cavity filling or excretion problems to better characterize the severity of pelvic floor pathologies or to be used for preoperative surgical planning.

1. Introduction

Pelvic floor disorders affect one fourth of adult women and the prevalence increases with age, up to 50% for women older than 80 years [1,2]. Some experts refer to these disorders as hidden epidemics to describe the extent of these diseases and their importance in the population [3]. Pelvic floor disorders may result from various factors such as aging, pregnancy, childbirth, obesity, or pelvic injuries [4]. They are mainly characterized by a weakening of the pelvic floor muscles and pelvic ligaments leading to a mechanical dysfunction of pelvic organ support structures. Symptoms are diverse and include urinary or bowel incontinence, sexual dysfunction and abnormal descent of pelvic organs.

Alongside routine clinical examination, magnetic resonance imaging (MRI) has emerged as an attractive non-invasive method for pelvic diagnosis [5]. Dynamic MRI examinations of pelvic tension exercise are considered essential [6] for the investigation of the pelvic area and clinical guidelines emphasize their importance to identify pathological organs deformations. Current clinical practice uses 2D dynamic MRI acquisition of a single sagittal plane during straining exercises that involve excretion to qualitatively assess the displacement and deformations of the main pelvic organs (bladder, uterus-vagina, or rectum). Radiologists inspect the displacement of the pelvic organs relative to bone-anchored lines, such as the pubococcygeal line [7]. Such explorations require manuals measurements to provide quantitative metrics. Beyond manual measurements, automated measurements of strain-induced deformation features were proposed to build a quantitative characterization of the pelvic organ dynamics to distinguish pathological cases from healthy ones [8] and to grade the severity of pelvic organ prolapses [9].

* Corresponding authors.
E-mail addresses: augustin.ogier@gmail.com, augustin.ogier@chuv.ch (A.C. Ogier), stanislas.rapacchi@univ-amu.fr (S. Rapacchi), marc-emmanuel.bellemare@univ-amu.fr (M.-E. Bellemare).

https://doi.org/10.1016/j.cmpb.2023.107569
0169-2607/

The visualization and characterization of pelvic dynamics by MRI has yet only been studied in the mid-sagittal plane. Although the majority of pelvic movements are identifiable in this plane, an estimation of 3D deformities may provide a complete assessment of the pelvic organs' mechanical defects. With limitations in acquisition speed using MRI, however, 3D imaging have been exclusive to static pelvic MRI to observe anatomy at rest during instructed apnea.

Ultrasound (US) has been used to observe organs during loading exercises [10], but remains limited due to image interpretation difficulties and restricted field of view. US sensors have evolved into a 3D and multi-planar imaging capability. However, despite its superior temporal resolution, moderate inter-observer agreement makes it difficult asses the effectiveness of 3D US for pelvic imaging over MRI [11]. In addition, although 3D US has reasonable agreement with MRI in detecting, for instance, major levator ani abnormalities [12,13], MRI offers superior soft tissue characterization and increased field of view, which makes it more suitable for the diagnosis of pelvis floor disorder in patients with multicompartmental involvement [14]. Recent attempts have been made to reconstruct pelvic organs in 3D from 3D ultrasonography, but current results are limited by the acquisition field and the difficult segmentation of these images. In [15], the authors depicted the use of B-Mode US in order to measure the volume of the bladder. The underlying model is based on a super ellipsoid. It provides a better measurement of the volume than the model used in routine, but it should not be appropriate for a more complex geometry such as those wanted for the observation of pelvic organ prolapse. To date, dynamic 2D MRI acquisitions have limited spatial coverage, which obviously depends on the position of the acquisition plane. We expect that an accelerated 4D MRI-based observation of the pelvic region could solve the main limitations identified above, with extended spatial coverage, while maintaining a sufficient temporal resolution for pelvic floor dynamics.

Although significant research has been performed, the pelviperineal physiology and the anatomic basis of pelvic floor diseases remain unclear [16,17]. This is the main reason repair surgery relapse is required [18]. To better comprehend the complete mechanical functioning of the pelvic floor non-invasively and to provide better post-operative support, biomechanical models have been proposed in recent years with the aim of providing patient-specific 3D simulations of the pelvic region [19,20]. Although pelvic system geometry could be known from high-resolution MRI images, patient-specific boundary conditions and material biomechanical properties are impossible to probe *in vivo* as it would require invasive procedures [21]. Thus, biomechanical numerical simulations may offer a proxy for characterization of pelvic organ mechanical impairment and guide surgical intervention. Geometric comparisons, based on shape descriptors and reference anatomical approximations, between biomechanical simulations and dynamic 2D sagittal MRI have been proposed to validate and enhance a physical model [22]. However, guiding 3D biomechanical models through a single 2D slice fails to fully simulate pelvic organs dynamics as simulation errors remain in off-plane areas [23]. Recent attempts to provide a finite elements based simulations of organ behavior still lack realistic 3D patient data [24].

There is a definite need for methods to generate dynamic 3D volumes of pelvic organs. Such approaches would allow full visualization of the 3D dynamics of pelvic organs in order to assist in the diagnosis or in the geometrical characterization of the actual 3D deformations of the pelvic organs. The characterization and the quantification of pelvic organ deformation observed in 3D will contribute to a quantitative evaluation of the disorders of the pelvic statics and will feed realistic data to biomechanical simulators that may improve the surgical management of pelvic organ prolapse. The analysis of MRI images and the segmentation of pelvic organs may also provide patient-specific 3D models to evaluate the pelvic dynamics in case of genital prolapse.

Pelvis straining MRI falls within real-time applications along with bolus-tracking perfusion MRI since the organs do not recover to the same position after each strain exercise and intracavity fluids can be excreted [6]. Patients cannot voluntarily strain their pelvis with the same intensity and regularity during repetitive cycles of forced breathing. Current state-of-the-art perfusion MRI methods rely on multi-slice (3 to 6) dynamic acquisitions in cardiac perfusion MRI, with an update rate of one heartbeat ($\approx$ 1 s) [25], or on 3D dynamic acquisitions such as liver perfusion MRI, with an update rate of few seconds per volume at best [26]. The clinically targeted high spatial resolution combined with the extreme nature of the pelvic organ unloading induced during these exercises has prevented real-time 3D pelvis MRI to date.

One frame per second mid-sagittal acquisitions are the current clinical consensus for exploration of the lesser pelvis region [6]. In this study, we aimed to achieve a 3D volume rate of several frames per second that would provide even better visualization of pelvic dynamics. For this purpose, we have used an ultra fast dynamic multi-planar acquisition that sparsely image the organ. To gain 3D information, it was necessary to complete the spatial information with a short temporal footprint to minimize errors due to deformations. For this purpose, we tested 3 spatial multi-slice configurations that can be easily reproduced in clinical setups. These configurations were implemented to estimate the organ tracking errors induced by prioritizing spatial coverage or spatial resolution. Comparison of these configurations helped to determine which configuration could provide superior visualization of the bladder and possibly even the main neighboring organs. When paired with a 3D static acquisition, the proposed acquisition aims to provide a volumetric dynamic reconstruction. This study was a completed extension of a previous seminal work [27].

Initially, the bladder was the focal point of our work as it is the simplest organ to consider being homologous to the sphere and easier to delineate due to its hyper signal in the images [28,29]. However, we have described our methodology in a generic way as we intend to apply it in future studies for the visualization of the uterus and rectum. We leveraged a semi-automated segmentation method, based on a fusion of image registration approaches, for the tracking of organs in the dynamic planes regardless of their spatial orientation. Linear interpolations on the geodesic path of each multi-planar segmentation have been proposed to refine the time scale inherited from the acquisition methods. Finally, we built dynamic 3D representations of organs through non-linear geometric registrations between each dynamic partial volume and the complete static volume of the high-resolution static acquisition. As this study produced dynamic 3D bladder volumes that can't be directly compared to a ground truth, we emphasized metrics that can be used to assess the adequacy of the volume reconstructions: 1) accuracy of the registration and 2) conservation of the bladder volume.

To our knowledge, this study was the first to propose both dynamic 3D+t visualization of the pelvic region during strain exercises and a dynamic 3D+t tracking of the organs. Furthermore, the organ reconstruction process allowed a characterization of the 3D deformations undergone by the pelvic organs during loading exercises. Analysis of the deformation fields allowing the reconstruction of organs, and more particularly the study of the resulting Jacobians, revealed local volume changes over time and provided a high-level 3D representation of the location of the highest strain areas on the organs surface. Specifically, analysis of Jacobians validated that our complete reconstruction methodology produced similar results between different geometric configurations of dynamic acquisitions.

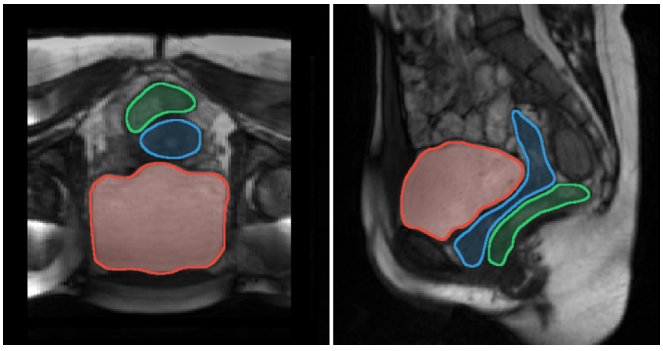

Fig. 1. Axial (left) and sagittal (right) views of pelvic floor acquired during a maximum expiration apnea with delineations of the major pelvic organs: bladder (red), uterus/vagina (blue), and rectum (green). (For interpretation of the references to colour in this figure legend, the reader is referred to the web version of this article.)

2. Methods

2.1. MRI Acquisitions

Both static and dynamic acquisition methods implemented in the context of this study were performed using a 1.5T MRI scanner (MAGNETOM Avanto, Siemens AG, Healthcare Sector, Erlangen, Germany) using a spine/phased array coil combination and T_1/T_2 weighted balanced steady-state free precession sequences (T_1/T_2W bSSFP). In comparison to the T_2W sequence commonly used for pelvic area MRI, the T_1/T_2W bSSFP sequence allows an optimal acquisition speed combined with a stark contrast between body fluids and the different pelvic organs tissues: uterus in dark gray, bladder in white (hyper-signal), and rectum and viscera in dark gray tissue and light gray content.

2.1.1. Static acquisition configuration

A quasi-isotropic 3D static image was acquired, as depicted in Fig. 1. High resolution and contrast in the sagittal plane allowed the anatomy of the pelvic region to be precisely delineated. The 3D T_1/T_2W bSSFP image (TR = 2.21 ms, echo time: 0.99 ms, flip angle: 32°, field of view: 277 mm × 320 mm × 88 mm, voxel size: 0.83 mm × 0.83 mm × 2.0 mm, GRAPPA = 2) was recorded during a maximum expiration apnea of 18 seconds. Acquisition was performed during apnea to allow precise 3D manual segmentation of the pelvic organs for use as references for the reconstruction scheme detailed in Section 2.5.

2.1.2. Dynamic acquisition configurations

Dynamic sequences provided a lower spatial resolution and a reduced contrast compared to static sequences, but allowed the monitoring of pelvic dynamics during organ loading exercises. Analysis of the biomechanical deformations induced during these exercises should therefore allow identification of elasticity defects in pelvic floor tissues. 3D dynamic MRI can be acquired either using slab excitations or multi-planar slice excitations. Due to the extended temporal footprint of 3D excitations (>1s), blurring can occur when observing rapid deformations. Thus, fast acquisition (≈ 100 ms) of multi-planar 2D slices was preferred to follow the motion of the pelvic organs. In this study, we sought to harness the potential of high-density coil arrays to accelerate MRI using parallel imaging techniques.

Non-linear reconstruction techniques, such as Compressed Sensing [30], were not considered in this preliminary work to maintain reliability of the imaging information and clinical transfer-ability. The sliding-window temporal-GRAPPA (TGRAPPA) technique [31] allowed for a significant acceleration. In TGRAPPA, consecutive images share low-frequency information to provide basis for image reconstruction. Pelvic deformations do not modify the low-frequency image information within the range of a second. Therefore, in this study, the full coverage of the pelvic region was guaranteed using up to a maximum of 12 slices within one second. Another interesting feature of this multi-planar setup is the T_1-recovery of the signal between images, which boosts signal-to-noise ratio and offers a reinforced contrast between tissues and liquids.

Table 1
Acquisition parameters of the three dynamic MRI sequences.

Configuration	C_{star}	C_{grid}	C_{lines}
Slice thickness (mm)	5	6	4
Number of cycles	100	100	60
Time repetition (ms)	2.9	2.6	1.9
Slice acquistion time (ms)	183.72	124.95	91.61
Field of view (mm)	302 × 350	300 × 350	299 × 350
In-plane resolution (mm)	1.09 × 1.09	1.36 × 1.36	1.82 × 1.82

2.1.3. Spatial order of dynamic acquisitions

Three dynamic sequences in multi-planar configurations were acquired, with three different geometric configurations that varied in number of planes and spatial locations but maintained the time for acquiring one set of all planes within 1s. We denoted the different geometries as C_{star}, C_{grid} and C_{lines} (cf. Fig. 2). The *Star* configuration consisted of one coronal plane, the mid-sagittal plane and two other planes which were oriented at about 45 degrees to the sagittal. The *Grid* configuration featured three sagittal and two coronal planes. The *Lines* configuration was made of several parallel sagittal planes covering the body from the right lateral side to the left lateral side. Regardless of the configuration, the number of planes from one acquisition cycle was noted N_p. For C_{star} and C_{grid}, N_p was equal to 4 and 5, respectively. The number of planes for C_{lines} was defined according to the corpulence of each subject to cover the pelvic area as much as possible and was typically set at 10 ($\pm$ 2).

2.1.4. Temporal order of dynamic acquisitions

In MRI, there is a close relationship between spatial resolution, temporal resolution and contrast of the acquired image. This leads to a trade-off where modification of one of these parameters induces a change in the others. Increasing the duration of a single image plane acquisition (*i.e.* the sequence-specific slice acquisition time [TS]) resulted in an image with improved contrast and better spatial resolution but lower temporal resolution. To follow the motions of the pelvic organs, an acquisition cycle (which acquired all planes consecutively) of less than a second had to be used. Defining the time-frame of a cycle by $N_p \cdot \mathrm{TS}$, each plane of a given configuration had thus to be acquired in less than $1/N_p$ seconds. Assuming the same field of view, the lower the N_p required by the geometric configuration, the longer the TS was, and therefore the more precise the spatial resolution, as detailed in the Table 1, and better the contrast, as illustrated in Fig. 3. To allow for a clinical-grade signal-to-noise ratio, the TS of C_{Lines} was set at a minimum of 110ms, even with a $N_p > 10$.

The number of cycles, N_c, acquired for each dynamic configuration was determined to set the total acquisition time (*i.e.* $N_p \cdot \mathrm{TS} \cdot N_c$) around 1:20 min in order to record several deformation phases of pelvic organs during loading exercises.

Regardless of dynamic configuration, for each $p \in [0\,;N_p[\subset \mathbb{N}$ (the spatial indexes of acquisition planes) we denoted $\mathcal{P}_p$ the set of the acquired planes $\{\mathcal{P}_p^k\}$ with $k \in [0\,;N_c[\subset \mathbb{N}$ the temporal index of the acquisition cycle.

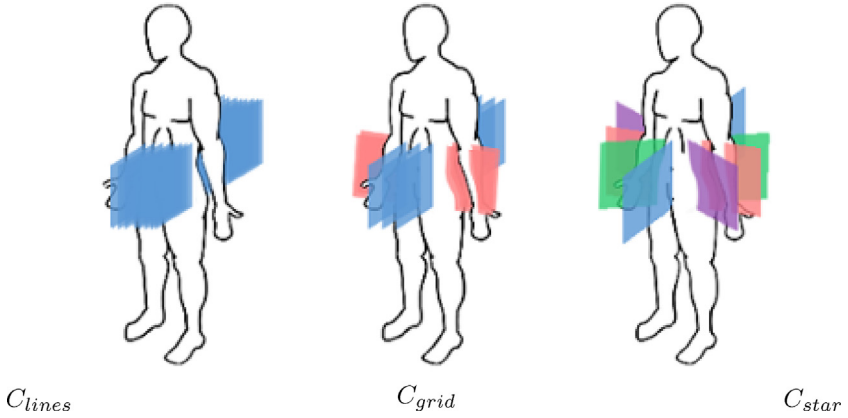

Fig. 2. Geometrical configuration of the planes for the three dynamic multi-planar acquisitions sequences.

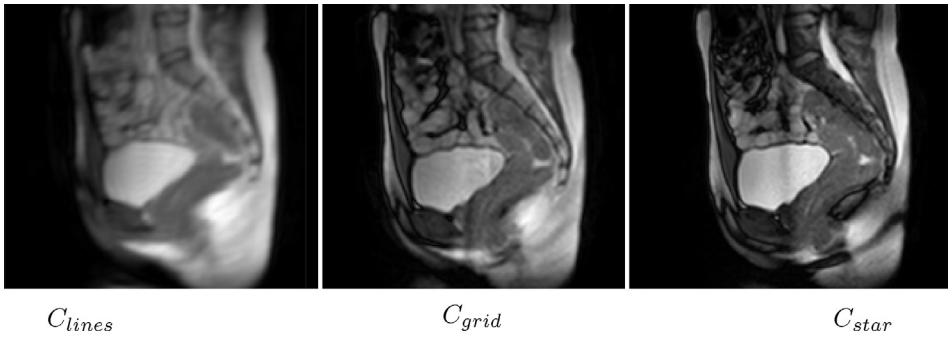

Fig. 3. Difference in contrast and resolution between similarly located sagittal planes from the different dynamic acquisition configurations.

2.2. Mathematical formalism

We introduce here the mathematical formalism of diffeomorphic registration widely used in the following sections. A diffeomorphism, ϕ, allows transformation of a target shape X towards a source shape Y, and allows identification of the correspondence between these two shapes, such as $\phi_x^t X \approx Y$. The shape X is warped into the new coordinate system by $\phi_x^t X = X \circ \phi(x,t)$, where the geodesic path $\phi(x,t)$ is described in [32]. The diffeomorphic function, $\phi(x,t)$, parameterized by time, $t \in [0,1]$ and x, spatial coordinate, is defined by $\delta\phi_x^t/\delta t = v_t(\phi_x^t)$ and $\phi_x^0 = \mathbf{Id}$, with $v(x,t)$ a time-dependent velocity field.

2.3. Pelvic organ segmentation

2.3.1. State of the art

Automatic segmentation of main pelvic organs is a challenging task due to overlapping MRI contrasts between the uterus, vagina, rectum and surrounding soft tissues. Only the bladder is natively contrasted due to the liquid it contains. Extrageneous liquid could be inserted in the pelvic cavities to enhance the contrast of the other organs, but, in this case, the clinical procedure would lose its non-invasive nature.

Several methods have been proposed for the segmentation of pelvic organs using MRI. Most of them have been designed for the segmentation of 3D static axial images [33–35] and only a few semi-automatic methods have already been developed for segmentation of dynamic 2D sagittal T_2W MRI images [9,28,36]. Although promising, these methods still require manual initialization and have not been able to obtain segmentation's with a average Dice similarity coefficient (DSC) greater than 0.90 for the bladder [9,28] or with a mean Hausdorff distance lower than 9 mm [36]. Recently, convolutional networks have shown good results in addressing the complex segmentation of pelvic organs in MRI but these most use static volumes [37]. Overall, the segmentation of multi-plane 2D dynamic MRI datasets is still challenging due to the combined non-rigid deformations and depleted contrasts. As a result, the segmentation process of pelvic organs has mainly been performed manually or semi-automatically in studies that have focused on pelvic dynamics [8,23].

2.3.2. Our method

In this study, the segmentation stage is the first step of a complete process allowing characterization of pelvic organ deformations (cf. Fig. 5). This step is crucial as incorrect segmentation leads to false deformation estimations. For the segmentation of pelvic organs, a semi-automated segmentation method was proposed on each set of 2D dynamic planes $\mathcal{P}_p$ independently, to balance between high segmentation accuracy and user's involvement. For each set of acquired planes $\mathcal{P}_p$, segmentation masks $\mathcal{M}_p$ were manually traced on a few slices, at fixed temporal intervals. The contours were then automatically propagated to all the remaining frames according to the method described in [38]. The manually segmented slices were denoted ${\mathcal{M}_p}^{i\cdot n}$, with $i \in \mathbb{N}$, and n the time step of the mandatory manual segmentation. According to our method, the manual segmentation of the slices ${\mathcal{M}_p}^{i\cdot n}$ and ${\mathcal{M}_p}^{(i+1)\cdot n}$ allowed the automatic segmentation of the $n-1$ slices of the interval using a fusion of different propagation schemes.

The propagation from one manually segmented slice ${\mathcal{M}_p}^{i\cdot n}$ to the next ${\mathcal{M}_p}^{(i+1)\cdot n}$ could be achieved, from an Eulerian perspective, by successively estimating the correspondence maps between the $n-1$ grey level $\mathcal{P}_p$ slices, pairwise. This process could be done in both forward and backward strategies depending on which slice was chosen to initiate the propagation. The forward strategy sought to estimate the diffeomorphism $\phi_{E_f}^k$, given by:

$$\phi_{E_f}^k = \phi_{v_f}^{i\cdot n+1} \circ \phi_{v_f}^{i\cdot n+2} \circ \ldots \circ \phi_{v_f}^k \quad (1)$$

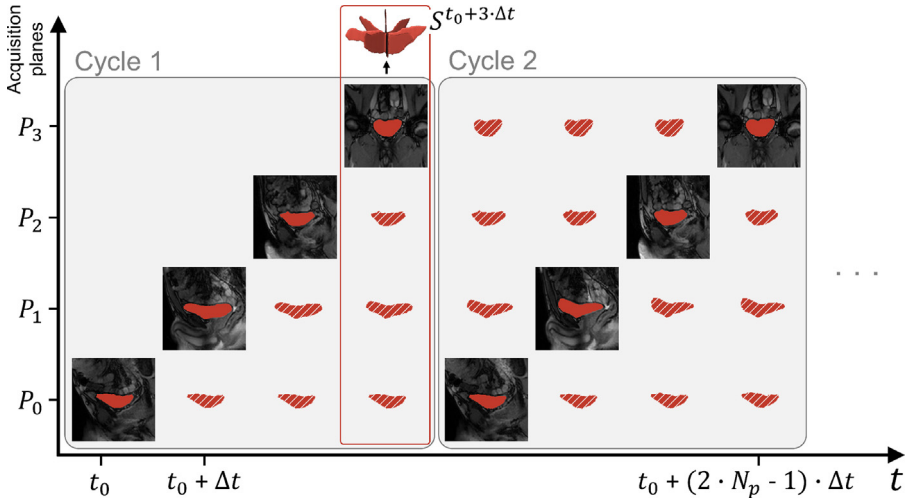

Fig. 4. Spatio-temporal configuration of the acquisition planes and temporal reconstruction scheme, illustrated for C_{star}. Filled segmentations refer to instants for which an image was acquired. Hatched segmentations correspond to the temporally reconstructed ones. All segmentations of all acquisition planes of a given instant t are combined to provide the skeleton S^t of the organ volume at that time.

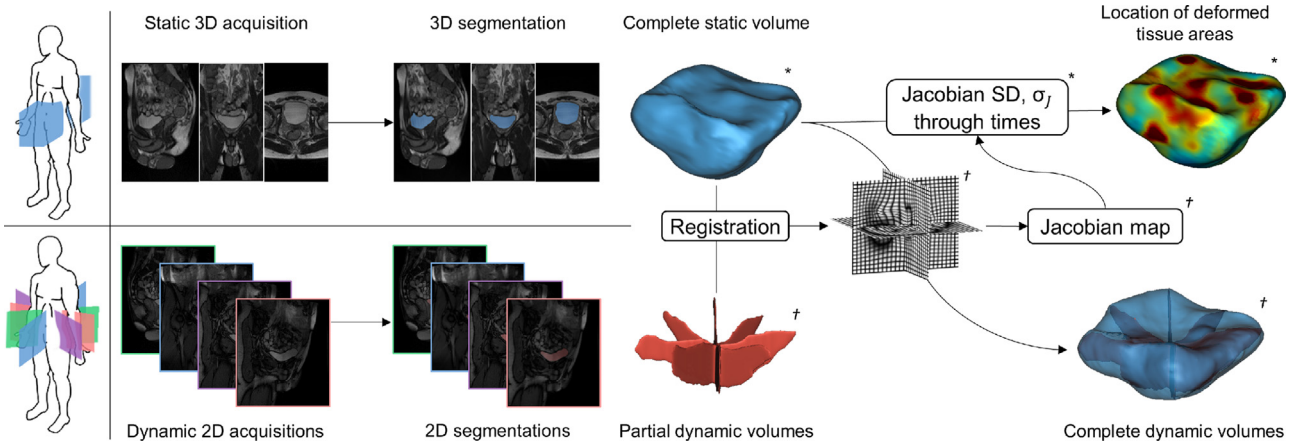

Fig. 5. Schematic overview of the reconstruction and characterization pipeline. Reconstruction of the dynamic volumes was achieved by registrating the 3D volume from the static acquisition to the partial volumes from the dynamic acquisitions, obtained after the temporal reconstruction process. The analysis of the resulting deformation fields over time provided the localization of the deformed tissue areas. * static entities, † dynamic entities.

where $\phi_{v_f}^j$ is the deformation field mapping $\mathcal{P}_p^{j-1}$ to $\mathcal{P}_p^j$. In a similar way, the backward strategy estimated $\phi_{E_b}^k$, given by the combination of the diffeomorphism $\phi_{v_b}^j$, mapping $\mathcal{P}_p^{j+1}$ to $\mathcal{P}_p^j$. Therefore, for $k \in]i \cdot n\,;(i+1)\cdot n[$ with $i \in \mathbb{N}$, the propagation to the missing segmentations M_p^k could have been performed by applying either $\phi_{E_f}^k \mathcal{M}_p^{i\cdot n}$ or $\phi_{E_b}^k \mathcal{M}_p^{(i+1)\cdot n}$. As registrations were performed between successive MRI slices, these Eulerian approaches did follow anatomical variations but rapidly diverged given that errors were accumulating with the number of ϕ_v^j combinations. Thus, accuracy decreased with respect to the distance from the starting slice. To minimize this divergence effect, the two approaches were merged and the missing segmentations were generated by:

$$\mathcal{M}_p^k = \left(\alpha_k \phi_{E_f}^k + \beta_k (\phi_{E_b}^k \circ \phi_{L_f})\right) M_p^{i\cdot n} \tag{2}$$

with ϕ_{L_f}, the deformation field resulting from the geometric registration between the two initial manually segmented masks. This diffeomorphism ϕ_{L_f} allowed performance of a reference frame shift, and merge the two Eulerian approaches. The determination of coefficients α_k and β_k were ruled by an arctan function to keep the high accuracy of each Eulerian propagation process near its propagation starting slice. The complete algorithm of the merging process and parametric details of the diffeomorphic registrations are available in [38]. All the segmentations were visually checked at the end of the process to ensure their quality.

2.4. Temporal reconstruction of segmentations

After the segmentation process, N_p datasets $\mathcal{M}_p^k$ were obtained, each with a cardinality of N_c. The next step towards the 3D reconstruction was to merge all M_p datasets into a unique set, $\mathcal{A}$, that we represented as a 2D matrix $[(t, p)]$. Taking t_0 as the instant of the first image, we denoted, $t = t_0 + k \cdot \Delta t$ with $\Delta t = \mathrm{TS}$. Such a matrix representation was chosen in order to correctly arrange each segmentation mask $\mathcal{M}_p^k$ according to the spatial and temporal parameters of the dynamic acquisitions. The spatial index p of each $\mathcal{M}_p^k$ indicated the temporal ordering of acquisition between all planes acquired within each acquisition cycle and k indexed the acquisition cycle. Therefore, as formulated in (3), each $\mathcal{M}_p^k$ was associated to $\mathcal{A}_p^{k\cdot N_p+p}$.

From our 2D acquisition scheme, only one plane of a given configuration C was available at a time t, as depicted in Fig. 4. As a consequence, for a plane position p, the segmentation masks had to be interpolated to fulfill the missing acquisition instants in a cycle. The missing segmentations in $\mathcal{A}_p^t$ were reconstructed by lin-

early interpolating along the geodesic path between the segmented mask of the previously acquired slice and the next one, as formalized in (3). We chose linear interpolating scheme on the geodesic path since the motion of pelvic organs is assumed to be continuous over the acquisition time of a cycle (less than 1 s).

$$\mathcal{A}_p^t = \begin{cases} \mathcal{M}_p^{(k//N_p)} & \text{if } p = k(\text{mod}\, N_p) \\ \mathcal{M}_p^{k'} \circ \phi(x, \frac{k-k'}{N_p}) & \text{otherwise} \end{cases}$$

$$\text{with} \quad \begin{aligned} \mathcal{M}_p^{k'} \circ \phi(x,1) &\approx \mathcal{M}_p^{k''} \\ k' &= \left((k-N_p)//N_p\right) \cdot N_p + p \\ k'' &= k' + N_p \end{aligned} \tag{3}$$

An illustration of the temporal reconstruction approach is given in Fig. 4 with the C_{star} configuration. The scheme is identical regardless of the configuration with abscissa values ranged from 0 to N_p and with t up to $(N_p \cdot N_c - 1)$. A horizontal line corresponds to the intermediate masks generated by interpolation between two actually segmented masks.

2.5. Three-dimensional isotropic volume reconstructions

The temporal interpolation provides several spatial and temporal samples of the considered organ. In Fig. 4, the aggregation of masks on a vertical line corresponds to the creation of what we call the *skeleton* of a dynamic volume at time t. All the masks belong to 2D spatial domains of the different acquisition planes. Therefore, the next step towards the 3D reconstruction of the dynamic volumes was to compute the affine transformations required to transfer the skeletons into a single 3D isotropic space. With all segmentations defined in the same 3D domain, volume skeletons S were generated at each instant t as the union of the segmentations from each acquisition plane at that time:

$$S^t = \bigcup_{p=0}^{N_p} \mathcal{A}_p{}^t \qquad \forall t \in [N_p - 1\,;\, N_p \cdot (N_c - 1) + 1] \tag{4}$$

Merging process was not performed for the first and last $N_p - 1$ volumes because segmentations were not available for all the acquisition planes at these instants (cf. Fig. 4).

As S^t are partial volumes, the final step towards the 3D reconstruction of the dynamic volumes was to complete these skeletons. To achieve the most natural and realistic reconstruction possible, a subject-specific approach was used. The 3D volume resulting from the segmentation of the finely resolved static acquisition was used as a template to be registered to each partial volume (cf. Fig. 5). The registration process involved two distinct steps to allow independent analysis of two significant biomechanical mechanisms in the study of pelvic organ disorders: organ displacement and organ deformation. First, organ displacement was estimated at each time by aligning the centers of mass of the static 3D volume to each dynamic partial volume. Then, a 3D nonlinear registration was performed between the prealigned volume contours. A nonlinear diffeomorphic model was chosen because of the need to register organs that might show dynamics with large deformations. To solve the many-to-few problem of matching complete to partial point clouds, a point/landmark-based similarity metric based on probabilistic estimate was used. Based on a bi-directional expected matching term between structures to be registered, the PSE metric introduced by Pluta *et al.* [39] minimized the distance between each point of a given point-set and the expected corresponding point from the other point-set. Let {V} be the set of points describing the contour of the complete static volume V_s and {R} the set of points describing the contour of a dynamic volume skeleton. Cardinalities of {V} and {R} were defined as m and r, respectively. Note that $r << m$, as {R} described the contour of a partially sampled volume. Our registration problem was therefore to minimize the objective function :

$$PSE(\{V\},\{R\}) = -\frac{1}{r}\sum_{i=1}^{r}\left\| R_i - \frac{1}{m}\sum_{j=1}^{m} G(R_i; V_j, \sigma_v) V_j \right\|^2 \tag{5}$$

with $G(R_i; V_j, \sigma_v)$ a normalized Gaussian with mean V_j and standard deviation σ_v. The standard deviation σ_v was empirically set to $1mm$. Implementation of the registration was performed using the BSpline SyN process of the ANTs library [40]. Registration processes produced 3D displacement vector fields $u^t = (u_x^t, u_y^t, u_z^t)$, for each instant t, enabling the mapping of the complete static volume V_s to each spatially undersampled dynamic volume S^t through the transformations $h^t = v + u^t(v)$ with v a voxel position set by $v = (v_x, v_y, v_z)$. Hence, for $t \in [N_p - 1\,;\, N_p \cdot (N_c - 1) + 1]$, each complete dynamic volume was generated using $V_s\left(v + u^t(v)\right)$ for each v.

2.6. Displacement and deformation characterization

The radiological interpretation of resultant 4D images can be tedious, thus a quantitative synthesis was sought to facilitate and standardize diagnosis. Taking advantage of the reconstruction process, two quantitative metrics may be directly extracted. The organ displacement recovered from the initial affine transformation may be a simple way to characterize organ movement. This metric remains crucial because clinical evaluation of the pelvic dynamics, and hence, the assessment of the pelvic floor disorders is routinely based on the observation of such anatomical landmarks [41]. Similar metrics have already been studied with classic 2D dynamic MRI [8,9] but to exploit the full potential of the three-dimensional aspect of the reconstruction, 3D organ deformations were analyzed using the deformation fields resulting from the non-linear registration.

Jacobian maps were computed to characterize 3D deformations. Let us denote the Jacobian matrix of h as Dh (with the $(i,j) - th$ element $\delta h_i/\delta v_j$). The Jacobian map, defined as the determinant of the Jacobian matrix $|Dh(v)|$, encoded the percentage of the dynamic local volume variations at each instant with respect to the static volume image (*i.e.* a value of 0.9 denotes 10% tissue loss, whereas 1.1 a 10% tissue increase). The quantity of deformations at each voxel of the organ for each instant t was therefore assessed through a Jacobian map $J^t(v) = \det\left(\delta h^t(v)/\delta v\right)$. The projection of each Jacobian map onto the surface of the static volume provided a visualization of the deformations undergone by the organ at the different phases of the loading exercises in a common domain. Information provided by all Jacobian maps has also been synthesized into a single map to facilitate the visualization of the deformation areas with a single representation. For this purpose, the σ_J map was calculated for which each voxel v represented the standard deviation (SD) of the values of each J^t map estimated across all t at v. Calculation was as follow:

$$\sigma_J(v) = \sqrt{\frac{1}{n}\sum_{t=0}^{n}\left(J^t(v) - \overline{J(v)}\right)^2} \tag{6}$$

with $n = N_c \cdot N_p - 2(N_p - 1)$, the number of dynamic volumes reconstructed. The σ_J map projected on a mesh of the reference static volume provided a high-level representation of the location of the most deformed tissue area during a dynamic acquisition sequence.

3. Results

3.1. Datasets

Pelvis areas of eight healthy participants (five women) were imaged. Subjects were 27.6 ± 3.8 years old and weighed 69.3 ±

11.0 kg. The static acquisition was recorded first during a maximum expiration apnea of 18 seconds. Afterwards, the three dynamic sequences in multi-planar configurations were acquired successively during forced breathing exercises of 1:20 minute each with a short rest between sequences. During these exercises, after 10 seconds of free breathing, the subjects alternately inspired and expired at maximum capacity. Subjects were also instructed to increase their pelvic pressure during the maximum inspiration and conversely to contract the pelvic floor during the expiration. These actions increased the intra-abdominal pressure, causing deformities of the pelvic organs. The study was approved by the local human research committee and was conducted in conformity with the Declaration of Helsinki.

Since no extrageneous liquid was injected into pelvic cavities in this study, only the segmentation of the bladder was straightforward, thus the analysis focused exclusively on this organ. For each subject, bladder volumes were generated at a rate of about 1/TS volumes per second. According to the configurations, 394, 492, and approximately 680 volumes were reconstructed for configurations C_{Star}, C_{Grid} and C_{Lines}, respectively, at a rate of about 5, 8, and 9 volumes per second. As the inspiration/expiration phases of subjects were not paced, the number of respiratory cycles fluctuated between successive dynamic acquisitions. Due to subject variability, from 4 to 12 inspiration/expiration phases were acquired. The average post-processing time for the complete methodology was around 18 min per reconstructed dynamic volume, regardless of the geometrical configuration.

Dynamic configuration C_{lines} has only been studied on 3 subjects due to a lack of resources that were needed to complete manual segmentation of the dynamic images.

Participants were instructed to go to the toilet 2 hours before the exam, to drink moderately up to 30 minutes before the exam, and then to fast so that the bladder would not fill during the exam. This way, organ volume did not vary between the different MRI sequences. Bladder volume of each subject was computed from the manual segmentation of the static acquisition. Subjects presented heterogeneous values ranging from 48 cm^3 to 403 cm^3.

3.2. Spatial discrepancy between segmentations from secant acquisition planes

Dynamic 2D segmentations were independently delineated on differently oriented planes. As only one plane could be imaged at a time, the segmentations from these planes naturally had a time offset between them (cf. Fig. 4). The evaluation of the discrepancy between segmentations from secant acquisition planes aimed to validate the relevance of the temporal reconstruction process (cf. Fig. 4) for the reduction of this temporal bias.

Let L_{ij} be the line defined as the intersection of two secant acquisition planes: $L_{ij} = \mathcal{P}_i \cap \mathcal{P}_j$. The intersection of L_{ij} with the segmentation mask $\mathcal{A}_i^t$ related to the plane $\mathcal{P}_i$ provided the set of points $I_{i,j}^t = \{L_{ij} \cap \mathcal{A}_i^t\}$. From this set, the inferior and the superior intersection points were denoted as $(I_{i,j}^t)^{sup}$ and $(I_{i,j}^t)^{inf}$, respectively. A schematic illustration is depicted in Fig. 6. In this figure, for visualization purposes, the two secant planes were taken at different times, each corresponding to one of the inspiration/expiration phases. In practice, during this study, distances between segmentation intersections remained narrower by leveraging the high speed of plane acquisitions.

Spatial discrepancy ζ between two segmentations from two secant planes was defined as the sum of the two Euclidean distances between the superior and inferior intersection points:

$$\zeta(\mathcal{A}_i, \mathcal{A}_j)^t = \left\| (I_{i,j}^t)^{sup} - (I_{j,i}^t)^{sup} \right\| + \left\| (I_{i,j}^t)^{inf} - (I_{j,i}^t)^{inf} \right\| \quad (7)$$

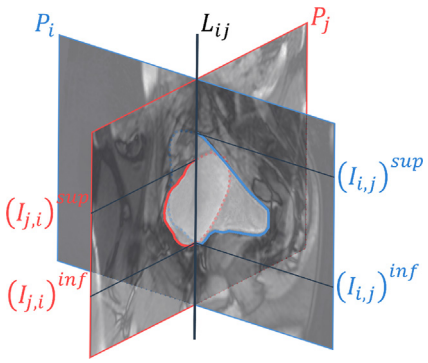

Fig. 6. Schematic illustration of the spatial inconsistency between two segmentations from two secant acquisition planes.

Spatial discrepancy was calculated between each pair of secant planes for each configuration except for C_{lines} (which was only composed of parallel planes). Spatial discrepancy scores for all subjects and all instances were 1.71 ± 1.24 mm for C_{star} and 2.51 ± 1.57 mm for C_{grid}, which corresponds to only a few pixels.

3.3. Consistency of three-dimensional reconstructions

The Bspline SyN registration implemented for the 3D reconstruction process was optimized as follows: the gradient step was 0.1 for each of the four multi-resolution levels with shrink factors of $\{6, 4, 2, 1\}$ and no smoothing sigmas. The number of iterations per level were $\{250, 200, 150, 100\}$ with a stepping out criterion based on a convergence threshold of 10^{-6} within 15 iterations. Knot spacing was set to 44 mm for the B-spline smoothing on the update displacement field at the base level which is reduced by a factor of two for each successive multi-resolution level. This yielded a final knot spacing of 5.5 mm. Such a low regularization scheme was retained because pelvic organ deformations are mostly global and no high frequency deformations had to be permitted in the registration process. Furthermore, this optimization preserved the overall topology of the template static organ. No restrictions were applied to the smoothing of the total displacement field as this did not improve the results.

Validation of the 3D organ reconstructions was a difficult process due to the lack of ground truth. Therefore, the evaluation focused on the consistency of the reconstructed volumes through two metrics: 1) accuracy of the registration and, 2) conservation of the bladder volume. Since the bladder is an in-compressible organ (filled with a liquid), its volume has to remain unchanged during the registration process when the static volume is deformed to match the shape of the partial dynamic volumes. Relative absolute volume deviation (RAVD) was computed at each instant between the reference volume and the reconstructed volume. The time averages of the values are displayed in Table 2. Average volume deviations were similar for all configurations with a mean value of 2.39% ± 2.16%. Subject 7 did not comply with the fluid consumption instructions prior to acquisition and therefore had the lowest bladder volume of all subjects, which could explain the outliers.

Evaluation of the mapping of the deformed static volume onto the organ volume skeletons provided the assessment of registration accuracy. For each point of the contour of the dynamic volume skeleton, the distance to the nearest point of the contour of the reconstructed volume was calculated. From these distances the maximum value and the average value described as the non-symmetric Hausdorff distance (HD) and the mean distance (MD), were extracted, respectively (Table 2). The average HD and MD over time reflected strong registration accuracy for all configurations with mean values of 2.19 ± 2.09 and 0.41 ± 0.31 mm, respectively. It

Table 2
Evaluation of three-dimensional reconstructions.

Configuration	Subject	RAVD (%)	HD (mm)	MD (mm)
C_{star}	#1	1.64 ± 1.47	1.37 ± 0.24	0.21 ± 0.06
	#2	1.88 ± 1.80	1.41 ± 0.28	0.18 ± 0.03
	#3	1.95 ± 1.41	1.36 ± 0.27	0.17 ± 0.04
	#4	2.82 ± 1.61	1.28 ± 0.22	0.18 ± 0.03
	#5	3.40 ± 0.94	1.33 ± 0.23	0.17 ± 0.02
	#6	1.66 ± 0.67	1.31 ± 0.23	0.16 ± 0.02
	#7	5.94 ± 3.31	1.32 ± 0.23	0.17 ± 0.02
	#8	1.58 ± 1.23	1.42 ± 0.29	0.19 ± 0.08
	Overall	**2.61 ±2.22**	**1.35 ±0.25**	**0.18 ±0.04**
C_{grid}	#1	2.70 ± 2.49	2.44 ± 0.68	0.45 ± 0.17
	#2	2.36 ± 2.12	2.07 ± 0.33	0.33 ± 0.09
	#3	2.63 ± 1.68	2.86 ± 0.63	0.65 ± 0.15
	#4	2.74 ± 2.13	1.76 ± 0.29	0.28 ± 0.07
	#5	1.26 ± 0.67	1.65 ± 0.28	0.23 ± 0.05
	#6	1.67 ± 1.03	1.82 ± 0.23	0.25 ± 0.05
	#7	2.00 ± 1.46	1.76 ± 0.35	0.25 ± 0.05
	#8	1.51 ± 1.21	1.75 ± 0.37	0.22 ± 0.09
	Overall	**2.11 ±1.79**	**2.01 ±0.58**	**0.33 ±0.17**
C_{lines}	#5	1.40 ± 0.91	3.60 ± 0.70	0.85 ± 0.15
	#6	1.03 ± 0.70	4.49 ± 0.89	1.07 ± 0.20
	#7	5.28 ± 2.85	3.31 ± 0.60	0.75 ± 0.14
	Overall	**2.57 ±2.62**	**3.80 ±0.90**	**0.89 ±0.21**

RVD = relative volume deviation, HD = Hausdorff distance, MD = mean distance. Values are mean ± standard deviation of all reconstructed volumes.

should be noted that comparison of the results between configurations must take into consideration that HD and MD were computed in the discrete 3D domains of the reconstructions. They were therefore directly related to their isotropic spatial resolution. As reported in Table 1, the voxel sizes were 1.09 mm for C_{star}, 1.36 mm for C_{grid} and 1.82 mm for C_{lines}. Expressed in voxels, the HD and MD values are quite similar between the configurations and equal to about 1 or 2 voxels.

3.4. High-level representation of pelvic organ deformation zones

Reconstructed volumes over skeletons and projections of the associated Jacobian maps are available for two subjects as supporting materials. Projections of the σ_J maps on meshes of the static reference volumes are shown in Fig. 7 for each subject and each configuration. Visualizations were performed using the Anatomist software [42]. At each point, the value for the intersection between the mesh of the static reference volume and the σ_J map, was estimated as the mean of the values within a sphere of 4 mm radius, almost 3 voxels, around the intersection point. This projection scheme was common to all configurations to provide a common reference for comparison regardless the resolutions of the reconstructed volumes. The reddest areas indicate the locations that underwent the largest deformations during the loading exercises. Note that volume scales are not the same for each subject in Fig. 7, *e.g.* bladder volume was 48 cm^3 for subject 7 whereas it was 403 cm^3 for subject 8.

Forced breathing exercises with maximum contraction are hardly reproducible for untrained subjects. Deformation magnitudes were different for each dynamic sequence and consequently differed for each geometric configuration *C*. For instance, in Fig. 7, subjects 4 and 5 did not exert the same intensities during each loading exercise explaining the main scale differences. On the whole, no visual correlation can be completed between the geometry configurations and amplitude of the deformations. Dynamic sequences with the highest deformation characteristics are C_{star} for subjects 1, 2, 7, and 8, C_{grid} for subjects 3, 4, and 5, and C_{lines} for subject 6. Intra-subject comparison of deformation amplitudes may not be relevant and was not the focus of our study. However, regardless of the load magnitude applied to the bladder, the intra-subject locations of the most deformed tissue areas are quite similar between dynamic sequences. Overall, tissue areas that have undergone deformities are located on the anterior and superior parts of bladders due to the abdominal viscera pushing against the bladder during loading exercises. Few deformation zones are visible on the inferior part due to a strong pelvic floor in our young healthy volunteers. Inferior deformations in patients could indicate pelvic floor weaknesses.

4. Discussion

While extensive research has been conducted on the movement of organs such as the brain [43] and heart [44], little work has been done on the analysis of the pelvic organ dynamics. Most of the studies have focused either on the realization of biomechanical simulators generated from 3D static acquisition [20], or on the characterization of organ deformations based on a single 2D dynamic slice [8,9]. Recently, Courtecuisse *et al.* [23] has proposed a registration approach to deform pelvic organs acquired in 3D static acquisitions using single-plane 2D dynamic acquisitions and *a priori* knowledge of boundary conditions and mechanical laws of the pelvic organs. This biomechanical knowledge was incorporated into the registration model because the ground truth information from a single 2D section is not enough to accurately guide organs that deform non-linearly in all 3 dimensions. This approach remains limited because it depends on pelvic tissue characterization, which remains unknown with high inter-subject variability, and the development of patient-specific models would require invasive procedures to probe the biomechanical properties *in vivo*.

In the proposed study, we provided 3D spatial coverage of the organs through the acquisition of several dynamic slices. Dynamic volumes were not simulated in a biomechanical sense and were reconstructed independently of any mechanical model. In addition, the subject-specific initial geometric model required for the 3D reconstruction process was readily available from a fast 3D static acquisition. Two possible static states were available for each subject from maximum inspiration or maximum expiration breath-hold. The latter was retained because it was the state closest to the natural condition of organs and, in pathological routines, will be less painful than inspiration. In further studies with patient recruitment, the deformation of the static model on dynamic volumes may require refinement to account for pelvic prolapse. This study

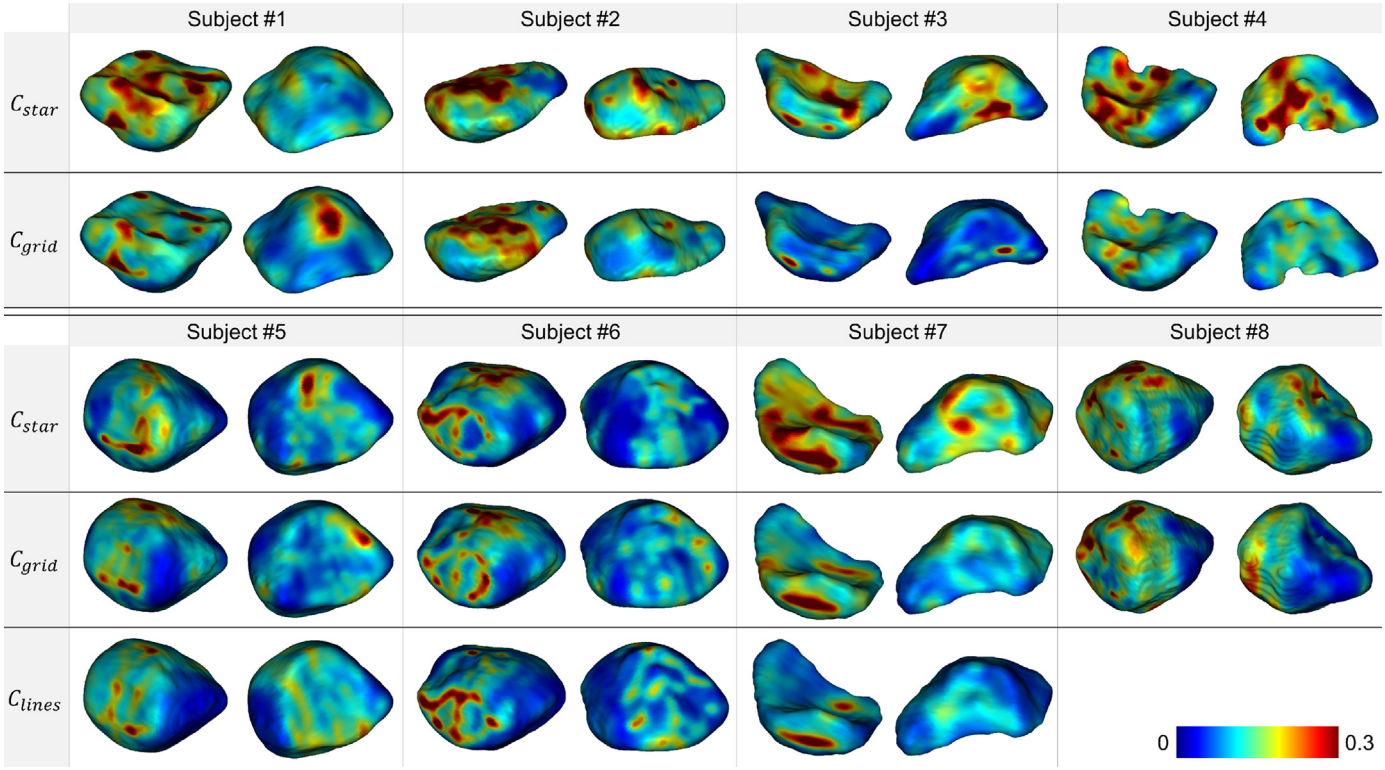

Fig. 7. Anterior (left) and posterior (right) views for each subject and configuration of the σ_J map projected on the corresponding reference static volumes. Reddest areas indicate the location of the highest strain areas on the organ surfaces during dynamic acquisition sequences.

emphasized the metrics to assess the adequacy of bladder reconstructions. Using these metrics, we demonstrated the appropriateness of the registration method for the reconstruction by preserving an average RAVD value around 2.5% and respecting the ground-truth contours provided by the all of the dynamic slices with average HD values of 2.2 $\pm$ 1.1 mm and average MD values of 0.4 $\pm$ 0.3 mm.

One limitation is the semi-automated segmentation that requires user interaction. For pelvic organs, existing automatic segmentation methods are generally dedicated to a specific type of dataset, either static 3D images or 2D axial or sagittal images. Most approaches are based on deformable models [28] which are rather difficult to parameterize even for one type of image. The proposed semi-automated method was the only hindrance to the fully automated aspect of our pipeline. Still, one of the originalities of our study was to propose dynamic acquisitions under different planes with open 3D geometric configurations. The advantages of the semi-automatic method that we proposed are manifold: First, the time spent to perform manual segmentation has been reduced by about 90% as only one in ten slices was manually segmented; Second, the proposed method is suitable on all planes, regardless of their orientation, resolution, or contrast. It adapts to all these acquisition parameters by propagating organ contours between similarly acquired slices. In future studies, such semi-automatic methods of segmentation will facilitate the creation of labeled datasets for 2D dynamic MRI and will allow investigation of the relevance of deep-learning methods for pelvic organ segmentation. To date, these approaches have been scarcely used and still provide insufficient results, with average DSC around 85% [45].

Within one acquisition cycle, planes were not acquired simultaneously. The spatial discrepancy ζ between the intersecting planes of the S^t skeletons was maintained low by temporally interpolating along the geodesic path between the bladder segmentations.

Dynamic volumes from each configuration could not be directly compared because subjects could not reproduce the same pelvic organ movements between each dynamic acquisition. The frequency of pushing phases and magnitude of the load applied to the organs were highly variable. Volumes and associated J maps, could not be compared one to one from one configuration to another. However, the higher-level σ_J maps allowed comparison of the spatial distribution of deformed tissue areas. For all subjects, the spatial distribution of deformed tissue regions was similar between configurations. Although the σ_J map has no direct physical meaning, its projection on the reference volume provided a preliminary mechanical characterization of the organs.

Overall, our processing pipeline proved to be compatible with all three configurations in terms of bladder reconstruction and deformation characterization, with equivalent end results. One of the three dynamic acquisition plane configurations can be chosen to ensure either complete spatial coverage (C_{lines}) or high spatial resolution (C_{star}). Combined with the proposed methodology, each configuration can provide a dynamic 3D+t representation of the bladder during loading exercises. The proposed pipeline is directly applicable in clinical settings and can be added to a routine examination as the acquisition time is minimal and the sequences are standard. In practice, only a 20 seconds static apnea sequence and a multi-planar acquisition of one straining exercise are necessary.

We have designed a complete methodology for the 3D+t representation of pelvic organs during loading exercises directly combined with a high-level 3D representation of the most strained areas on the organ surfaces. To our knowledge, this study is the first to propose a dynamic 3D real-time observation of the pelvic region as well as a 3D representation of the organs' deformations. Our proposal opens novel perspectives towards real-time dynamic

3D+t pelvic imaging and biomechanical pelvic organs characterization.

In this study, three different geometrical configurations of dynamic multi-planar acquisitions have been proposed to provide the first 4D representation of pelvic organs. Two of them were particularly original, C_{star} and C_{grid}, because they were composed of planes oriented differently from the sagittal plane (typically imaged in clinics). In this study, we verified that all three configurations could provide deformation characterizations. In consequence, the choice of a multi-planar configuration depends on the preference for spatial coverage or spatial resolution. In clinical practice, it may be easier to configure C_{lines}, but configuring C_{star} should also be straight-forward and may enable improved visualization of smaller structures.

To allow a direct transfer to clinics, only the acceleration methods available on the clinical machines were considered. However, the recently developed simultaneous multislice acquisition would allow the simultaneous acquisition of several parallel planes at the same time [46]. Future studies will be conducted with the ethical authorization to inject extraneous liquid into the rectal and vaginal cavities in order to segment all pelvic organs and study the complete pelvic dynamics. This framework will be integrated in a more global evaluation of the disorders of the pelvic statics taking into account all the organs of the pelvic floor whose finality is to develop a personalized and reliable numerical model of the disorders of the pelvic statics. In the long term, the analysis will allow a better understanding of pathophysiology by obtaining easily understandable 3D dynamic models, leading to a change in clinical practice. The aim of such global evaluation would be to determine new risk factors of pelvic failure, to target the operative indications, to help corrective surgery in case of complex or recurrent prolapses and to possibly impact future operative techniques. The ability to obtain dynamic 3D+t volumes also allows the development of more advanced 3D shape descriptors [47] to better characterize the degree of severity of pelvic pathologies for diagnostic assistance.

Supporting materials caption

Animations describing the volume deformations of 2 observed bladders. Global displacement is not reproduced, but colormap provided a visualization of the local surface changes. First column: reconstruction of the 3D dynamic volumes (blue) on the skeletons from the multi-slice acquisition segmentations (red). Second column: Projection on the static volume of the Jacobian maps associated with the registrations generating the reconstructed complete dynamic volumes. Third column: Single projection of the σ_J map on the static volume. Volumes from each geometric configuration were placed in a common time frame but the volume rate per second is different and each configuration was imaged during independent acquisition. For each representation, the anterior (left) and posterior (right) views are provided.

Declaration of Competing Interest

All authors have participated in (a) conception and design, or analysis and interpretation of the data; (b) drafting the article or revising it critically for important intellectual content; and (c) approval of the final version.

This manuscript has not been submitted to, nor is under review at, another journal or other publishing venue.

The authors have no affiliation with any organization with a direct or indirect financial interest in the subject matter discussed in the manuscript

Acknowledgements

This study was ethically approved by the following institutional review board: “comité de protection des personnes Sud-Ouest et Outre-Mer1”, from September 21st 2020, ID RCB : 2020-A00673-36. This research did not receive any specific grant from funding agencies in the public, commercial, or not-for-profit sectors. The authors would like to thank Katerina Eyre for constructive criticism of the manuscript.

Supplementary material

Supplementary material associated with this article can be found, in the online version, at 10.1016/j.cmpb.2023.107569

References

[1] I. Nygaard, M.D. Barber, K.L. Burgio, K. Kenton, S. Meikle, J. Schaffer, C. Spino, W.E. Whitehead, J. Wu, D.J. Brody, et al., Prevalence of symptomatic pelvic floor disorders in us women, JAMA 300 (11) (2008) 1311–1316.
[2] J.M. Wu, C.P. Vaughan, P.S. Goode, D.T. Redden, K.L. Burgio, H.E. Richter, A.D. Markland, Prevalence and trends of symptomatic pelvic floor disorders in us women, Obstet. Gynecol. 123 (1) (2014) 141.
[3] J.O. DeLancey, The hidden epidemic of pelvic floor dysfunction: achievable goals for improved prevention and treatment, Am. J. Obstet. Gynecol. 192 (5) (2005) 1488–1495.
[4] B.H. Gurland, G. Khatri, R. Ram, T.L. Hull, E. Kocjancic, L.H. Quiroz, R.F. El Sayed, K.R. Jambhekar, V. Chernyak, R.M. Paspulati, et al., Consensus definitions and interpretation templates for magnetic resonance imaging of defecatory pelvic floor disorders, Int. Urogynecol. J. 32 (10) (2021) 2561–2574.
[5] C.A. Woodfield, S. Krishnamoorthy, B.S. Hampton, J.M. Brody, Imaging pelvic floor disorders: trend toward comprehensive mri, Am. J. Roentgenol. 194 (2010) 1640–1649.
[6] R.F. El Sayed, C.D. Alt, F. Maccioni, M. Meissnitzer, G. Masselli, L. Manganaro, V. Vinci, D. Weishaupt, ESUR, E.P.F.W. Group, et al., Magnetic resonance imaging of pelvic floor dysfunction-joint recommendations of the esur and esgar pelvic floor working group, Eur. Radiol. 27 (5) (2017) 2067–2085.
[7] H. Zhang, Z. Wang, X. Xiao, J. Wang, B. Zhou, Dynamic magnetic resonance imaging evaluation before and after operation for pelvic organ prolapse, Abdomin. Radiol. 47 (2) (2022) 848–857.
[8] M. Rahim, M.-E. Bellemare, R. Bulot, N. Pirró, A diffeomorphic mapping based characterization of temporal sequences: application to the pelvic organ dynamics assessment, J. Math. Imaging Vis. 47 (1–2) (2013) 151–164.
[9] I. Nekooeimehr, S.K. Lai-Yuen, P. Bao, A. Weitzenfeld, S. Hart, Automated contour tracking and trajectory classification of pelvic organs on dynamic mri, J. Med. Imag. 5 (1) (2018) 014008.
[10] G. Salsi, I. Cataneo, G. Dodaro, N. Rizzo, G. Pilu, M.S. Gascòn, A. Youssef, Three--dimensional/four-dimensional transperineal ultrasound: clinical utility and future prospects, Int. J. Womens Health 9 (2017) 643.
[11] C.S. Calderwood, A. Thurmond, A. Holland, B. Osmundsen, W.T. Gregory, Comparing 3d ultrasound to 3d mri in the detection of levator ani defects, Female Pelvic Med. Reconstruct. Surg. 24 (4) (2018) 295.
[12] K.J. Notten, K.B. Kluivers, J.J. Fütterer, K.J. Schweitzer, J. Stoker, F.E. Mulder, R.G. Beets-Tan, R.F. Vliegen, P.M. Bossuyt, R.F. Kruitwagen, et al., Translabial three-dimensional ultrasonography compared with magnetic resonance imaging in detecting levator ani defects, Obstetric. Gynecol. 124 (6) (2014) 1190–1197.
[13] D.O. El-Haieg, N.M. Madkour, M.A.A. Basha, R.A. Ahmad, S.M. Sadek, R.M. Al–Molla, E.F. Tantwy, H.N. Almassry, K.M. Altaher, N.E. Mahmoud, et al., Magnetic resonance imaging and 3-dimensional transperineal ultrasound evaluation of pelvic floor dysfunction in symptomatic women: a prospective comparative study, Ultrasonography 38 (4) (2019) 355.
[14] R. Nardos, A. Thurmond, A. Holland, W.T. Gregory, Pelvic floor levator hiatus measurements: mri versus ultrasound, Urogynecology 20 (4) (2014) 216–221.
[15] M.-L. Chang, H.-C. Li, C.-K. Liu, H.-S. Chiang, C.-C. Hsu, Novel three-dimensional bladder reconstruction model from b-mode ultrasound image to improve the accuracy of bladder volume measurement, Sensors 21 (14) (2021) 4893.
[16] A.M. Weber, H.E. Richter, Pelvic organ prolapse, Obstetric. Gynecol. 106 (3) (2005) 615–634.
[17] C. Maher, B. Feiner, K. Baessler, C. Schmid, Surgical management of pelvic organ prolapse in women, Cochrane Database Syst. Rev. (4) (2013).
[18] H. Abed, D.D. Rahn, L. Lowenstein, E.M. Balk, J.L. Clemons, R.G. Rogers, S.R.G. of the Society of Gynecologic Surgeons, et al., Incidence and management of graft erosion, wound granulation, and dyspareunia following vaginal prolapse repair with graft materials: a systematic review, Int. Urogynecol. J. 22 (7) (2011) 789–798.
[19] M.-E. Bellemare, N. Pirro, L. Marsac, O. Durieux, Toward the simulation of the strain of female pelvic organs, in: 2007 29th Annual International Conference of the IEEE Engineering in Medicine and Biology Society, IEEE, 2007, pp. 2752–2755.

[20] Z.-W. Chen, P. Joli, Z.-Q. Feng, M. Rahim, N. Pirró, M.-E. Bellemare, Female patient-specific finite element modeling of pelvic organ prolapse (pop), J. Biomech. 48 (2) (2015) 238–245.
[21] C. Rubod, M. Brieu, M. Cosson, G. Rivaux, J.-C. Clay, L. de Landsheere, B. Gabriel, Biomechanical properties of human pelvic organs, Urology 79 (4) (2012) 968–e17.
[22] M. Rahim, M.-E. Bellemare, N. Pirró, R. Bulot, A quantitative approach for the assessment of the pelvic dynamics modeling, IRBM 32 (5) (2011) 311–315.
[23] H. Courtecuisse, Z. Jiang, O. Mayeur, J. Witz, P. Lecomte-Grosbras, M. Cosson, M. Brieu, S. Cotin, Three-dimensional physics-based registration of pelvic system using 2d dynamic magnetic resonance imaging slices, Strain (2020) e12339.
[24] M.T. Gordon, J.O.L. DeLancey, A. Renfroe, A. Battles, L. Chen, Development of anatomically based customizable three-dimensional finite-element model of pelvic floor support system: pop-sim1.0, Interface Focus 9 (4) (2019) 20190022, doi:10.1098/rsfs.2019.0022.
[25] S. McElroy, G. Ferrazzi, M.S. Nazir, K.P. Kunze, R. Neji, P. Speier, D. Stäb, C. Forman, R. Razavi, A. Chiribiri, et al., Combined simultaneous multislice bssfp and compressed sensing for first-pass myocardial perfusion at 1.5 t with high spatial resolution and coverage, Magn. Reson. Med. 84 (6) (2020) 3103–3116.
[26] L. Feng, L. Axel, H. Chandarana, K.T. Block, D.K. Sodickson, R. Otazo, Xd-grasp: golden-angle radial mri with reconstruction of extra motion-state dimensions using compressed sensing, Magn Reson Med 75 (2) (2016) 775–788.
[27] A.C. Ogier, S. Rapacchi, A. Le Troter, M.-E. Bellemare, 3d dynamic mri for pelvis observation-a first step, in: 2019 IEEE 16th International Symposium on Biomedical Imaging (ISBI 2019), IEEE, 2019, pp. 1801–1804.
[28] R. Namías, M.-E. Bellemare, M. Rahim, N. Pirró, Uterus segmentation in dynamic mri using lbp texture descriptors, in: Medical Imaging 2014: Image Processing, volume 9034, International Society for Optics and Photonics, SPIE, 2014, pp. 1009–1017, doi:10.1117/12.2043617.
[29] H. Marc-Adrien, P. Nicolas, B. Marc-Emmanuel, et al., Combining loss functions for deep learning bladder segmentation on dynamic mri, in: 2021 IEEE EMBS International Conference on Biomedical and Health Informatics (BHI), IEEE, 2021, pp. 1–4.
[30] M. Lustig, D. Donoho, J.M. Pauly, Sparse mri: the application of compressed sensing for rapid mr imaging, Magn. Reson. Med. 58 (6) (2007) 1182–1195.
[31] F.A. Breuer, P. Kellman, M.A. Griswold, P.M. Jakob, Dynamic autocalibrated parallel imaging using temporal grappa (tgrappa), Magn. Reson. Med. 53 (4) (2005) 981–985.
[32] M.F. Beg, M.I. Miller, A. Trouvé, L. Younes, Computing large deformation metric mappings via geodesic flows of diffeomorphisms, Int. J. Comput. Vis. 61 (2) (2005) 139–157.
[33] D. Pasquier, T. Lacornerie, M. Vermandel, J. Rousseau, E. Lartigau, N. Betrouni, Automatic segmentation of pelvic structures from magnetic resonance images for prostate cancer radiotherapy, Int. J. Radiat. Oncol.* Biol.* Phys. 68 (2) (2007) 592–600.
[34] C. Duan, Z. Liang, S. Bao, H. Zhu, S. Wang, G. Zhang, J.J. Chen, H. Lu, A coupled level set framework for bladder wall segmentation with application to mr cystography, IEEE Trans. Med. Imag. 29 (3) (2010) 903–915.
[35] Z. Ma, R.M.N. Jorge, T. Mascarenhas, J.M.R. Tavares, Segmentation of female pelvic organs in axial magnetic resonance images using coupled geometric deformable models, Comput. Biol. Med. 43 (4) (2013) 248–258.
[36] Z. Jiang, J.-F. Witz, P. Lecomte-Grosbras, J. Dequidt, C. Duriez, M. Cosson, S. Cotin, M. Brieu, B-Spline based multi-organ detection in magnetic resonance imaging, Strain 51 (3) (2015) 235–247.
[37] D. Nie, L. Wang, Y. Gao, J. Lian, D. Shen, Strainet: spatially varying stochastic residual adversarial networks for mri pelvic organ segmentation, IEEE Trans. Neural Netw. Learn. Syst. 30 (5) (2018) 1552–1564.
[38] A. Ogier, M. Sdika, A. Foure, A. Le Troter, D. Bendahan, Individual muscle segmentation in mr images: a 3d propagation through 2d non-linear registration approaches, in: Engineering in Medicine and Biology Society (EMBC), 2017 39th Annual International Conference of the IEEE, IEEE, 2017, pp. 317–320.
[39] J. Pluta, B.B. Avants, S. Glynn, S. Awate, J.C. Gee, J.A. Detre, Appearance and incomplete label matching for diffeomorphic template based hippocampus segmentation, Hippocampus 19 (6) (2009) 565–571.
[40] N.J. Tustison, B.B. Avants, Explicit b-spline regularization in diffeomorphic image registration, Front. Neuroinform. 7 (2013) 39.
[41] M. Kobi, M. Flusberg, V. Paroder, V. Chernyak, Practical guide to dynamic pelvic floor mri, J. Magn. Reson. Imaging 47 (5) (2018) 1155–1170.
[42] D. Rivière, D. Papadopoulos-Orfanos, J. Régis, J.-F. Mangin, A structural browser of brain anatomy, Neuroimage 11 (5) (2000).
[43] S. Bauer, R. Wiest, L.-P. Nolte, M. Reyes, A survey of mri-based medical image analysis for brain tumor studies, Phys. Med. Biol. 58 (13) (2013) R97.
[44] H. Wang, A.A. Amini, Cardiac motion and deformation recovery from mri: a review, IEEE Trans. Med. Imag. 31 (2) (2011) 487–503.
[45] F. Feng, J.A. Ashton-Miller, J.O. DeLancey, J. Luo, Convolutional neural network-based pelvic floor structure segmentation using magnetic resonance imaging in pelvic organ prolapse, Med. Phys. (2020).
[46] S. Rapacchi, T. Troalen, Z. Bentatou, M. Quemeneur, M. Guye, M. Bernard, A. Jacquier, F. Kober, Simultaneous multi-slice cardiac cine with fourier-encoded self-calibration at 7 tesla, Magn. Reson. Med. 81 (4) (2019) 2576–2587.
[47] K. Makki, A. Bohi, A.C. Ogier, M.-E. Bellemare, A new geodesic-based feature for characterization of 3d shapes: application to soft tissue organ temporal deformations, in: 2021 25th International Conference on Pattern Recognition, IEEE, 2021.